Antierosion in a 90° Bend by Particle Impaction

J. R. Fan, J. Yao, and K. F. Cen
Institute of Thermal Power Engineering and CE&EE, Zhejiang University,
Hangzhou 310027, People's Republic of China

Ribbed bend protection, a new method to protect duct bends against erosion in gas–solid flows, was studied theoretically. In this method, ribs are evenly welded on the outer wall of the inside bend at 20°–80°, and the material of the bend is medium carbon steel. An experimental system is set up to perform 3-D numerical work simultaneously. Experimental and numerical results agree well and confirm that the method is simple and efficient for erosion protection. Numerical simulation is used to study the axial gas-flow characteristics along the bend and the secondary flow at the cross section. Detailed analyses involving the impact of velocity and the incidence angle of particle–metal (particle-rib or particle-duct) impact show the mechanism of the antierosion effect. As a result, both experimental and theoretical predications demonstrate that the average erosion rate of ribbed bends is only one-third of the bare bend under test conditions, and that rectangular ribs possess greater antierosion ability than square ribs do. Besides, the predictions suggest that the erosion of the wall is more serious than that of the ribs on a ribbed bend, while the wear distribution pattern remains unchanged after adding ribs at the bend.

Introduction

The gas–solid flow in curved ducts is frequently encountered in engineering problems, for example, coal injection into entrained-flow gasifiers, cyclone separators and classifiers, pneumatic conveying of powders in transport lines, sandblasting, and high-velocity fluidization, as in circulating fluidized beds and other equipment. However, solid particles pneumatically transported through curved ducts will impact on the bend wall and may cause serious erosion problems, threatening machine reliability by increasing the vibration level, shortening the service life of the equipment, even leading to structural failure. A previous study by Tilly (1979) showed that under the same test conditions, the erosion rate of a bend could be 50 times higher than that of a straight duct. Therefore, protecting bends from erosion is always an urgent task in gas–solid flow systems.

Factors affecting erosion

Erosion of a solid surface by particles has been the subject of many studies (Finnie, 1972; Humphrey, 1990). In general, the extent of surface erosion by the impingement of abrasive particles depends on the following factors: (1) system operation conditions (such as impinging velocity, impact angle, particle number density at impact, and properties of the carrier fluid); (2) nature of target materials (such as material properties, duct orientation and curvature, and surface condition); (3) properties of impacting particles (such as type of particles, mechanical properties, size and sphericity). Of these factors, the first group has been shown to be the most important for evaluating erosion potential. As far as the same particles and target material are concerned, a decrease in the momentum of the impacting particles or a change in the impact angle can greatly reduce the duct erosion rate.

Methods for erosion protection

Currently, several methods are used to reduce erosion in gas–solid flows:

1. Reducing particle loading from the flow. For example, installing a dust remover or filter. While effective, this method increases equipment cost and requires the regular exchange of dust remover or filter components. Besides, it is impossible to eliminate all the fine particles. When conveying particles pneumatically, the solid phase itself is an actuating medium and should not be removed.

Correspondence concerning this article should be addressed to J. R. Fan.

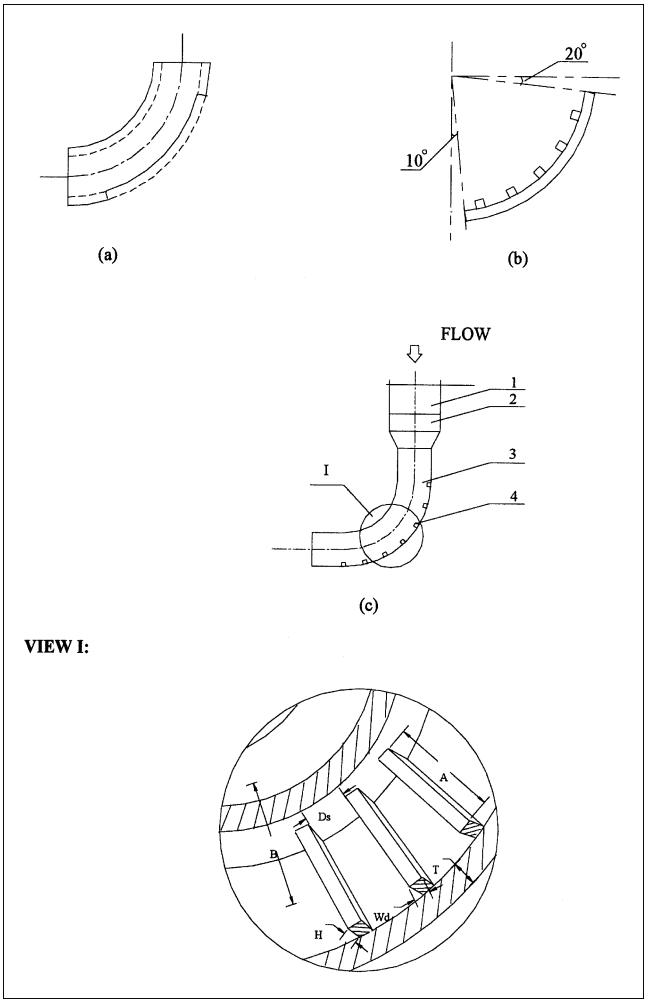

Figure 1. Experiment model design.

(a) Bend specimen picture 1; (b) bend specimen picture 2; (c) experiment model schematic drawing: (1) inlet pipe (Φ30); (2) variable diameter joint; (3) test model (□20); (4) bend specimen. VIEW I—A: 20 mm; B: 20 mm; T: 5 mm; Wd; H; Ds: refer to Table 2.

2. Locating the position of a major erosion zone and coating a high-hardness alloy or applying a protective lining (such as alumina cement, diabase, or middle manganese nodular cast iron) in that particular area. However, this often leads to a large increase in the cost of manufacture.

3. Optimizing equipment design by keeping particle velocity and the impinging angle out of the serious erosion range. This method requires detailed knowledge of gas–solid flows, but its application is usually limited by flow conditions and design requirements.

The present article studies a new method, in which a number of ribs with a certain cross-sectional shape are fixed on the outer wall of the inside duct bend (Figure 1). Fan et al. (1992) introduced a finned-tube erosion method of protection. Song et al. (1996) have demonstrated that a ribbed straight pipe would reduce erosion. The ribbed bend reduces erosion by changing the pattern of particle movement, altering the impingement angle, and reducing impact velocity.

The distribution of erosion wear on the surface of the bend requires a numerical solution that gives the particle velocity and the position history. With this information, an erosion model can be applied to estimate the erosion inside the bend. This article solves the governing equations coupled with the second-order turbulence model (k-ϵ equations) for a three-dimensional turbulent gas flow field in body-fitted coordinates (BFC). The prediction of particle trajectories in the turbulent flow inside the duct takes into account the effect of turbulence by using a stochastic particle-dispersion model (Fan et al., 1997). In this article, the impact and rebound model (Grant and Tabakoff, 1975) and the erosion model (Tabakoff et al., 1979) are used to predict particle rebounding and local erosion rate.

In a previous study, the authors (Yao et al., 2000) showed that this protecting technique is very effective for Perspex duct bends, with ribs fixed on the entire bending area and the straight section extending beyond it. The present article is an extension of that work, both in numerical simulation and in experiments, where a medium carbon steel bent duct is employed. The ribs are evenly fixed onto the wall along outer bend from 20° to 80°.

Experimental Details

Apparatus and instruments

To examine the erosion rate, experiments were performed by ribbing the bend's outer surface at regular intervals. The ribs were evenly distributed in 20°–80° angles with the front point of the bend. According to the rib's cross section, ribbed bends are divided into six kinds known as A–F-group. A,B,C-group bends have ribs with a square cross section, that is, 5×5, 4×4, 3×3 (unit: mm$\times$mm), respectively, and D,E,F-group bends have ribs with a rectangle cross section, that is, 5×2.5, 4×2, 3×2 (unit: mm$\times$mm), respectively. In each group, the ribbed bends are divided into four sections by their ribs' intervals, which are determined by the ratio to the ribs' height. According to our previous research (Yao et al., 2000), the four ratios chosen in the present experiment are 1.5, 2.5, 4, and 6. For example, in the A-group bends, the ribs' height is 5 mm and the intervals between them will be: 7.5 mm at a ratio of 1.5 (A1); 12.5 mm at 2.5 (A2); 20 mm at 4 (A3); and 30 mm at 6 (A4). Therefore, for six groups of ribbed bends, there are 24 different cases in all.

The experimental setup is shown in Figure 2. The erosion tunnel consists of a long bend, into which the particles are fed at a controlled rate. The particles move along with the gas to reach a steady velocity before impacting on the target specimens at the test section. Each specimen was tested three times. The gas flow rate was kept constant during each test. In order to reduce measurement error, each specimen was accurately weighed with a precision balance and washed in acetone before measurement.

The abrasive material used in these experiments was pulverized coal, a common fuel fired in power plants, sieved to the desired size distribution. The targets were made of medium carbon steel, which has been widely used in China as a pipeline material.

Experiment Parameters. The experiment parameters are outlined in Table 1.

Specimens Design. The test piece is shown in Figure 1, and the geometric data for the ribs are given in Table 2.

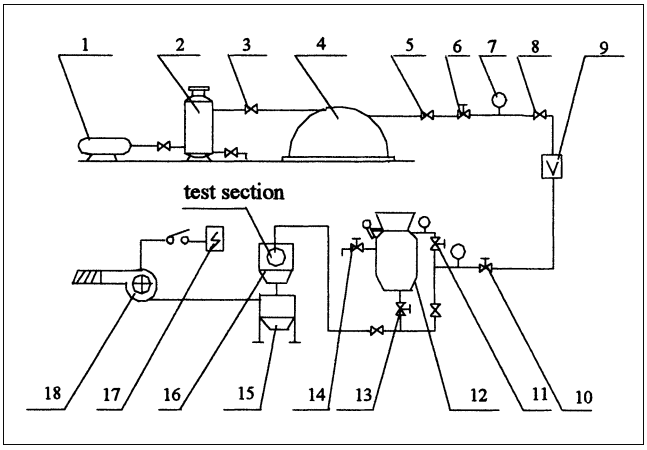

Figure 2. Overall experiment system.

(1) Air compressor; (2) oil–water separator; (3) stop valve; (4) gas reservoir; (5) stop valve; (6) compressed-air filtering reduce pressure valve (QPJ-1 type); (7) pressure gauge; (8) stop valve; (9) glass rotor flowmeter (LZB-50 type); (10) stop valve; (11) stop valve; (12) pneumatic convey store pump; (13) stop valve; (14) exhaust valve; (15) revolving wind separator; (16) specimen sealed chamber; (17) power supply; (18) blower.

Erosion State of Specimens. The erosion state on the surface of the bare specimen is much more serious than that of the ribbed ones. For the bare specimen, there were clear wavy strips engraved on the surface, the most serious erosion occurring at about 30°–40° and 70°–80°, which coincides with the numerical results in the latter half of the present article. On the other hand, there is no clear erosion scar on the surface of the ribbed specimen. There is so little erosion on ribbed specimens that they appear to be as new as the original ones. No hole or worn place appeared on any of the specimens by the end of the test.

Numerical Method and Models

Assumptions

The following assumptions are made in the model:

1. The two-phase (air–solids) flow in the vertical bend is in steady state, and fully developed.

2. The gas phase (air) is Newtonian, incompressible, and isothermal. The gas-phase momentum equation can be considered elliptic.

Table 1. Summary of Prediction Conditions

Parameter	Value or Range
Particle arithmetic mean diameter $\bar{d}_p$ (μm)	50
Particle diameter range d_p (μm)	20 ~ 80
Gas volume flow Q_v (m^3/h)	30
Volume flow Q_s with standard state (m^3/h)	59.2769
Crack degree, Ω	0.99673
Reynolds number, Re_g	8.826×10^4
Cross section of square duct A_s (mm^2)	20×20
Fluid average velocity, Vm (m/s)	41.2
Volume density of solids, Cv	0.327%
Weight density of solids, Cw	84.483%
Two-phase mixture density ρ_m (kg/m^3)	7.74
Bend curvature, R/D	3

Table 2. Bend Specimens Comprehensive Data Table

Specimens	H (mm)	Wd (mm)	Ds/H	H/D_L	AR	Rib No.
A1	5	5	1.5	0.25	1	5
A2	5	5	2.5	0.25	1	4
A3	5	5	4	0.25	1	4
A4	5	5	6	0.25	1	3
B1	4	4	1.5	0.2	1	6
B2	4	4	2.5	0.2	1	5
B3	4	4	4	0.2	1	4
B4	4	4	6	0.2	1	3
C1	3	3	1.5	0.15	1	8
C2	3	3	2.5	0.15	1	6
C3	3	3	4	0.15	1	4
C4	3	3	6	0.15	1	3
D1	5	2.5	1.5	0.25	2	5
D2	5	2.5	2.5	0.25	2	4
D3	5	2.5	4	0.25	2	4
D4	5	2.5	6	0.25	2	3
E1	4	2	1.5	0.2	2	8
E2	4	2	2.5	0.2	2	5
E3	4	2	4	0.2	2	4
E4	4	2	6	0.2	2	3
F1	3	2	1.5	0.15	1.5	10
F2	3	2	2.5	0.15	1.5	7
F3	3	2	4	0.15	1.5	5
F4	3	2	6	0.15	1.5	4
O						0

3. The solid phase is composed of 20–80-μm spheres with a Gaussian size distribution. The particles are present as a dilute phase that is free of interparticle collisions. However, particle–wall impacts are considered. Particle rotation and electrostatic forces are negligible.

All the geometric parameters involved in this model are determined from experimental data (Table 1). Therefore, numerical predictions can be readily compared with the measurement data.

Solution domain

The detailed geometry of the bend and flow field are shown in Figure 3. The gas-phase simulation uses the body-fitted coordinates. Three grid levels, with $20\times10\times68$, $20\times10\times82$,

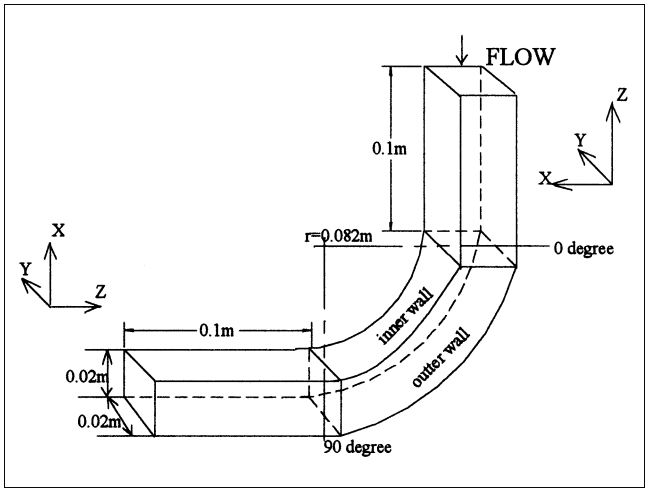

Figure 3. Bend and solution domains of the flow field.

Table 3. Grid Levels Applied in Samples

Grid Levels	X	Y	Z	Straight Part in Z	Curved Part in Z	Application
$20\times10\times68$	20	10	68	10	58	*O*, *A*, *D*
$20\times10\times82$	20	10	82	10	72	*B*, *E*
$20\times10\times106$	20	10	106	10	96	*C*, *F*

and $20\times10\times106$ control volumes, respectively, are used, depending on the rib size. The $20\times10\times68$ grids are used for the bare bend marked O, as well as ribbed bends A and D. There are 20 intervals in the x-direction, 10 in the y-direction, and 68 in the z-direction, with 10 intervals in the straight section and 58 in the curved section. There are other cases that are analogous to this one, as shown in Table 3.

Figure 3, however, does not give the geometry of the ribs for each individual case. Rib size and arrangement are listed in Table 2 and illustrated Figure 1, respectively. The flow between the ribs is also assumed to be incompressible, steady state, and with fully developed turbulence.

Governing equations for gas-phase flow

The gas-phase flow calculations were performed by the Eulerian approach, based on the time-averaged Navier–Stokes equations coupled with the well-known k-ϵ turbulence model (Launder and Spalding, 1974). It takes into account the source terms, resulting from the momentum exchange with the dispersed phase, using the so-called particle-source-in-cell (PSI-IN-cell) method (Crowe et al., 1977). In the present article, physical objects are described in the (ξ, η, ζ) BFC system.

The general form of the elliptic differential equations governing a three-dimensional flow is given by

$$\frac{\partial}{\partial\xi}(U\phi)+\frac{\partial}{\partial\eta}(V\phi)+\frac{\partial}{\partial\zeta}(W\phi) = \frac{1}{Re}\left\{\frac{\partial}{\partial\xi}\left[\Gamma\left(q_1\frac{\partial\phi}{\partial\xi}+q_2\frac{\partial\phi}{\partial\eta}+q_3\frac{\partial\phi}{\partial\zeta}\right)\right]\right\} + \frac{\partial}{\partial\eta}\left[\Gamma\left(q_2\frac{\partial\phi}{\partial\xi}+q_4\frac{\partial\phi}{\partial\eta}+q_5\frac{\partial\phi}{\partial\zeta}\right)\right] + \frac{\partial}{\partial\zeta}\left[\Gamma\left(q_3\frac{\partial\phi}{\partial\xi}+q_5\frac{\partial\phi}{\partial\eta}+q_6\frac{\partial\phi}{\partial\zeta}\right)\right]+\boldsymbol{SJ} \quad (1)$$

where U, V, and W represent the three velocity components in body-fitted coordinates. The source terms of the gas phase and the effective viscosity, Γ, are summarized in Table 4 for different variables, ϕ. The equations are solved simultaneously using the finite-volume differential method (Patankar, 1980) together with the boundary conditions. Here

$$\frac{\partial\underline{V}}{\partial x}=\frac{\partial\underline{V}}{\partial\xi}\xi_x+\frac{\partial\underline{V}}{\partial\eta}\eta_x+\frac{\partial\underline{V}}{\partial\zeta}\zeta_x$$
$$\frac{\partial\underline{V}}{\partial y}=\frac{\partial\underline{V}}{\partial\xi}\xi_y+\frac{\partial\underline{V}}{\partial\eta}\eta_y+\frac{\partial\underline{V}}{\partial\zeta}\zeta_y$$
$$\frac{\partial\underline{V}}{\partial z}=\frac{\partial\underline{V}}{\partial\xi}\xi_z+\frac{\partial\underline{V}}{\partial\eta}\eta_z+\frac{\partial\underline{V}}{\partial\zeta}\zeta_z$$
$$\underline{V}=u,v,w \quad (2)$$

where, u, v, and w can be replaced by U, V, and W through the following algebraic transformation

$$U=(u\xi_x+v\zeta_y+w\xi_z)J$$
$$V=(u\eta_x+v\eta_y+w\eta_z)J$$
$$W=(u\zeta_x+v\zeta_y+w\zeta_z)J \quad (3)$$

where J denotes the Jacobi exchange determinant

$$J=\begin{vmatrix} x_\xi\ldots y_\xi\ldots z_\xi \\ x_\eta\ldots y_\eta\ldots z_\eta \\ x_\zeta\ldots y_\zeta\ldots z_\zeta \end{vmatrix} \quad (4)$$

Defined below are q_1 through q_6

$$q_1=(\xi_x^2+\xi_y^2+\xi_z^2)J^2; \qquad q_2=(\eta_x\xi_x+\eta_y\xi_y+\eta_z\xi_z)J^2;$$
$$q_3=(\zeta_x\xi_x+\zeta_y\xi_y+\zeta_z\xi_z)J^2; \quad q_4=(\eta_x^2+\eta_y^2+\eta_z^2)J^2;$$
$$q_5=(\zeta_x\eta_x+\zeta_y\eta_y+\zeta_z\eta_z)J^2; \quad q_6=(\zeta_x^2+\zeta_y^2+\zeta_z^2)J^2. \quad (5)$$

The values for the constants are $C_1=1.47$; $C_2=1.92$; $C_\mu=0.09$; $\sigma_k=1.0$; $\sigma_\epsilon=1.3$.

It should be noted that different coordinate systems are used in the numerical solution, that is, BFC coordinates for the gas phase and Cartesian coordinates for the solid phase. Upon introduction of the solid phase, a coordinate transfer procedure is required to transform every variable from BFC coordinates into Cartesian ones.

Lagrangian formulation for the particles

The solid phase uses the Lagrangian approach, in which the particles are followed along their trajectories through the flow field.

The equations of particle motion in a three-dimensional Cartesian coordinate system are given below

$$\frac{dx_p}{dt}=u_p, \quad \frac{dy_p}{dt}=v_p, \quad \frac{dz_p}{dt}=w_p \quad (6)$$

$$\frac{du_p}{dt}=\frac{1}{\tau}(u_g-u_p)-g, \quad \frac{dv_p}{dt}=\frac{1}{\tau}(v_g-v_p)$$
$$\frac{dw_p}{dt}=\frac{1}{\tau}(w_g-w_p) \quad (7)$$

where x_p, y_p, and z_p are the location of a particle in the x, y, z directions, respectively; u_g, v_g, w_g and u_p, v_p, w_p are the instantaneous velocities of the gas and the particle phases, respectively; and $\tau=\rho_p d_p^2/18\mu f$ is the particle relaxation time, where $f=C_D/(24/Re)$. The drag coefficient, C_D, is defined by Sommerfeld and Zivkovic (1994) as

$$C_D=\frac{24}{Re_p}f_p$$

Table 4. Diffusion and Source Terms

Parameter, ϕ	Diffusion, Γ	Source, S
1	0	0
u	μ/J	$S^u = -\left(\frac{\partial P}{\partial \xi}\xi_x + \frac{\partial P}{\partial \eta}\eta_x + \frac{\partial P}{\partial \zeta}\zeta_x\right) + \frac{1}{Re}\left[\frac{\partial}{\partial \xi}\left(\mu\frac{\partial u}{\partial x}\right)\xi_x + \frac{\partial}{\partial \eta}\left(\mu\frac{\partial u}{\partial x}\right)\eta_x + \frac{\partial}{\partial \zeta}\left(\mu\frac{\partial u}{\partial x}\right)\zeta_x + \frac{\partial}{\partial \xi}\left(\mu\frac{\partial v}{\partial x}\right)\xi_y + \frac{\partial}{\partial \eta}\left(\mu\frac{\partial v}{\partial x}\right)\eta_y + \frac{\partial}{\partial \zeta}\left(\mu\frac{\partial v}{\partial x}\right)\zeta_y + \frac{\partial}{\partial \xi}\left(\mu\frac{\partial w}{\partial x}\right)\xi_z + \frac{\partial}{\partial \eta}\left(\mu\frac{\partial w}{\partial x}\right)\eta_z + \frac{\partial}{\partial \zeta}\left(\mu\frac{\partial w}{\partial x}\right)\zeta_z\right]$
v	μ/J	$S^v = -\left(\frac{\partial P}{\partial \xi}\xi_y + \frac{\partial P}{\partial \eta}\eta_y + \frac{\partial P}{\partial \zeta}\zeta_y\right) + \frac{1}{Re}\left[\frac{\partial}{\partial \xi}\left(\mu\frac{\partial u}{\partial y}\right)\xi_x + \frac{\partial}{\partial \eta}\left(\mu\frac{\partial u}{\partial y}\right)\eta_x + \frac{\partial}{\partial \zeta}\left(\mu\frac{\partial u}{\partial y}\right)\zeta_x + \frac{\partial}{\partial \xi}\left(\mu\frac{\partial v}{\partial y}\right)\xi_y + \frac{\partial}{\partial \eta}\left(\mu\frac{\partial v}{\partial y}\right)\eta_y + \frac{\partial}{\partial \zeta}\left(\mu\frac{\partial v}{\partial y}\right)\zeta_y + \frac{\partial}{\partial \xi}\left(\mu\frac{\partial w}{\partial y}\right)\xi_z + \frac{\partial}{\partial \eta}\left(\mu\frac{\partial w}{\partial y}\right)\eta_z + \frac{\partial}{\partial \zeta}\left(\mu\frac{\partial w}{\partial y}\right)\zeta_z\right]$
w	μ/J	$S^w = -\left(\frac{\partial P}{\partial \xi}\xi_z + \frac{\partial P}{\partial \eta}\eta_z + \frac{\partial P}{\partial \zeta}\zeta_z\right) + \frac{1}{Re}\left[\frac{\partial}{\partial \xi}\left(\mu\frac{\partial u}{\partial z}\right)\xi_x + \frac{\partial}{\partial \eta}\left(\mu\frac{\partial u}{\partial z}\right)\eta_x + \frac{\partial}{\partial \zeta}\left(\mu\frac{\partial u}{\partial z}\right)\zeta_x + \frac{\partial}{\partial \xi}\left(\mu\frac{\partial v}{\partial z}\right)\xi_y + \frac{\partial}{\partial \eta}\left(\mu\frac{\partial v}{\partial z}\right)\eta_y + \frac{\partial}{\partial \zeta}\left(\mu\frac{\partial v}{\partial z}\right)\zeta_y + \frac{\partial}{\partial \xi}\left(\mu\frac{\partial w}{\partial z}\right)\xi_z + \frac{\partial}{\partial \eta}\left(\mu\frac{\partial w}{\partial z}\right)\eta_z + \frac{\partial}{\partial \zeta}\left(\mu\frac{\partial w}{\partial z}\right)\zeta_z\right]$
k	$\mu/(J\cdot\sigma_k)$	$\sigma_k/Re - \epsilon$
ϵ	$\mu/(J\cdot\sigma_\epsilon)$	$C_1\epsilon G_k/(kRe) - C_2\epsilon$

where

$$Re_p = \frac{\rho D_p |V_g - V_p|}{\mu}; \quad f_p = 1 + 0.15 Re_p^{0.687}$$

$$\text{for } Re_p \le 1{,}000; \quad f_p = 0.0183 Re_p, \quad \text{for } Re_p > 1{,}000 \quad (8)$$

To consider the effect of gas-phase turbulence on particle dispersion, the instantaneous gas velocities u_g, v_g, w_g are given in terms of the time-averaged gas velocities U_g, V_g, W_g, calculated from Eq. 1, and the fluctuating velocities u'_g, v'_g, w'_g

$$u_g = U_g + u'_g, \quad v_g = V_g + v'_g, \quad w_g = W_g + w'_g \quad (9)$$

The gas-phase fluctuation velocities in a particular eddy are simulated by a random Fourier series

$$u'_g = \sum_{i=1}^{N} R_1 U_i \cos\left(\omega_i t - R_2 \alpha_i^u\right)$$

$$v'_g = \sum_{i=1}^{N} R_3 V_i \cos\left(\omega_i t - R_4 \alpha_i^v\right)$$

$$w'_g = \sum_{i=1}^{N} R_5 W_i \cos\left(\omega_i t - R_6 \alpha_i^w\right) \quad (10)$$

where $R_1 - R_6$ are random numbers with a Gaussian distribution; U_i, V_i, and W_i are amplitudes of fluctuation corresponding to the frequency ω, which can be determined experimentally from the turbulence energy spectrum of the gas–solid flow concerned; and a_i^u, a_i^v, and a_i^w are the initial phase angle in the x, y, and z directions, respectively.

A particle is assumed to interact with an eddy over a certain period of time, which is the lesser of the eddy lifetime and the transition time. The fourth-order Runge–Kutta scheme with adaptive step length was used to solve Eq. 7, given the initial particle location and velocity.

Particle-size distribution

The particles were grouped into "parcels," the smallest collections of particles retaining the physical properties of the solid phase, with a Gaussian size distribution

$$f(D_p) = \frac{1}{\sqrt{2\pi}} \exp\left(-\frac{(D_p - D_m)^2}{2D_n^2}\right)$$

where

$$D_m = \frac{D_{\max} + D_{\min}}{2.0} \quad D_n = \frac{D_{\max} - D_{\min}}{4.0} \quad (11)$$

with

$$D_{\max} = 80\ \mu m, \text{ and } D_{\min} = 20\ \mu m$$

Because of the stochastic nature of the particle–wall collision, a large number of particles must be traced in order to obtain a representative distribution of the particle collision frequency over the duct section. In the present work, 50 particle trajectories were calculated for each of the 200 starting locations uniformly distributed across the inlet plane, generating a total of 10,000 particle trajectories.

Impact and rebound

Particle rebound from a wall has been studied experimentally by Grant and Tabakoff (1975). The change in particle momentum due to impact is found to be mainly a function of the particle impact velocity V and its incidence angle β. The following empirical correlations are used for the impact restitution ratio

$$\frac{V_{n_2}}{V_{n_1}} = 1.0 - 0.4159\beta_1 - 0.4994\beta_1^2 + 0.292\beta_1^3 \qquad (12)$$

$$\frac{V_{t_2}}{V_{t_1}} = 1.0 - 2.12\beta_1 + 3.0775\beta_1^2 - 1.1\beta_1^3 \qquad (13)$$

where V_n and V_t represent the particle velocity impact components normal and tangential to the wall, respectively; subscripts 1 and 2 refer to the conditions before and after impact, respectively; and β_1 (in radians) is the angle between the incident velocity and the tangent to the surface.

Wall mass erosion prediction

Experimental results reported by Tabakoff et al. (1979) indicate that erosion of a target material depends on the particle-impact velocity and impingement angle. Measurements of the erosion rate were made for coal ash particles impacting on a steel surface. An empirical correlation was established for the erosion mass parameter, E, which is defined as the ratio of the mass loss of the target to the mass of the impinging particles

$$E = K_1\left\{1 + C_K\left[K_2 \sin\left(\frac{90}{\beta_0}\beta_1\right)\right]\right\}^2 W_1^2 \cos^2\left(1 - R_1^2\right) + K_3(W_1 \sin \beta_1)^4 \qquad (14)$$

where W_1 and β_1 are the impact velocity and impingement angle, respectively; $R_1 = 1 - 0.0016W_1 \sin \beta_1$; $\beta_0 = 20°$ is the angle of maximum erosion; $C_K = 1$ (for $\beta_1 \le 3\beta_0$); $C_K = 0$ (for $\beta_1 > 3\beta_0$); K_1, K_2, and K_3 are constants due to material properties; and $K_1 = 1.505101 \times 10^{-6}$, $K_2 = 0.296007$, $K_3 = 5.0 \times 10^{-12}$.

Results and Discussion

To facilitate the discussion, two important parameters are defined, erosion rate and relative erosion rate.

The *erosion rate* is defined as $E = \Delta M_s/M_a$, that is, the ratio of the eroded mass of wall material, ΔM_s, to the mass of the impacting abrasive particles, M_a. Here, E is a function of particle impact velocity and impacting angle; it helps to describe the extent of erosion of a specimen. The erosion rate can be substantially reduced by effective protective measures.

The *relative erosion rate*, E/E_0, is defined as the ratio of the erosion rate, E, of a ribbed bend to that of the uncovered bend, E_0. This reduced parameter shows the effectiveness of ribbing for erosion reduction.

Besides, in the present article, the erosion rate refers to the sum of the rib and the bend-wall erosion rates: E_f refers to the erosion rate of the ribs; E_w refers to the erosion rate of the bend wall; and E is the sum of E_f and E_w.

Comparison between predictions and measurement data

Figure 4 compares numerical predictions with experimental results.

The average relative erosion rate, obtained from measurement data for all ribbed bends, is 0.335356, while the predicted value is 0.335335, suggesting an excellent agreement.

Gas-phase flow

Figure 5 illustrates the gas flow in the axial direction in the bend. Gas flow in the axial direction in a bare bend is smooth and fully developed, and has a high velocity throughout the bend (Figure 5a). However, it becomes more complicated in a ribbed bend, because of the turbulence produced by the ribs (Figures 5b–5d, sampled from B1). Compared to a bare bend, the velocity of the bulk gas flow in the axial direction in a ribbed bend is higher, though the velocity of the turbulent flow between ribs is much lower. The axial gas flow in the rib intervals is like a rolling wheel, and so, plays an important role in erosion reduction.

The influence of a secondary flow at the cross section in the duct bend is also considered in the present article. For both the ribbed bend and the smooth bend (Figures 6a and 6b), the speed of the secondary flow is much lower in comparison with their own axial gas flow. In particular, the high speed of the secondary flow is located near both side walls, while the speed of the secondary flow in the middle of the cross section is obviously low. Consequently, the secondary flow will play only a small part in determining the particle trajectory under the present conditions.

Particle trajectories

Figure 7 shows the particle trajectories in the bends. In the bare bend, particles will not only slide and roll along the outer bend but also impact on it with high speed by inertial and centrifugal forces (Figures 7a and 7b). Fine particles may not impact on the wall throughout the bend, while coarser particles collide with the wall more than once. A large particle may first impact on the outer bend soon after entering it, then rebound from the wall with sufficient speed to move into the bulk flow. After gaining enough momentum there, it impacts on the outer bend near its end.

The trajectories of particles in ribbed bends are far more complicated than those in the bare bend (Figures 7c and 7d). Most particles may make primary or secondary impacts on the first rib (Figure 7e), then rebound into the bulk flow with considerable momentum. The second and later ribs (Figures 7e and 7f) will also be impacted by particles, whose rebounds

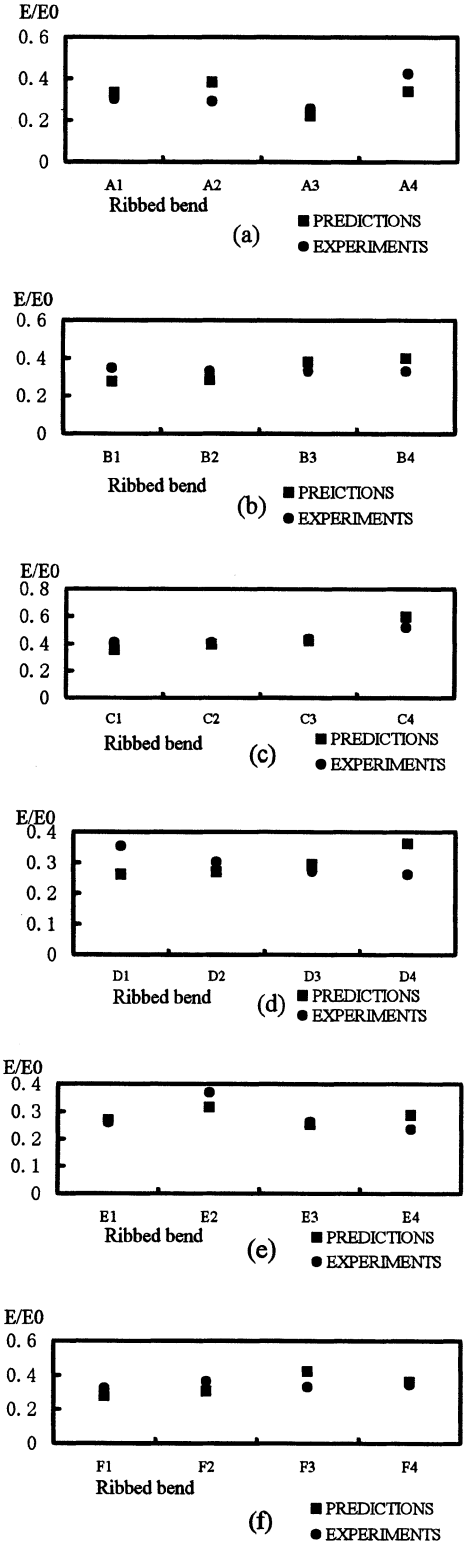

Figure 4. Predictions vs. experiments.

(a) A-Group ribbed bends; (b) B-group ribbed bends; (c) C-group ribbed bends; (d) D-group ribbed bends; (e) E-group ribbed bends; (f) F-group ribbed bends.

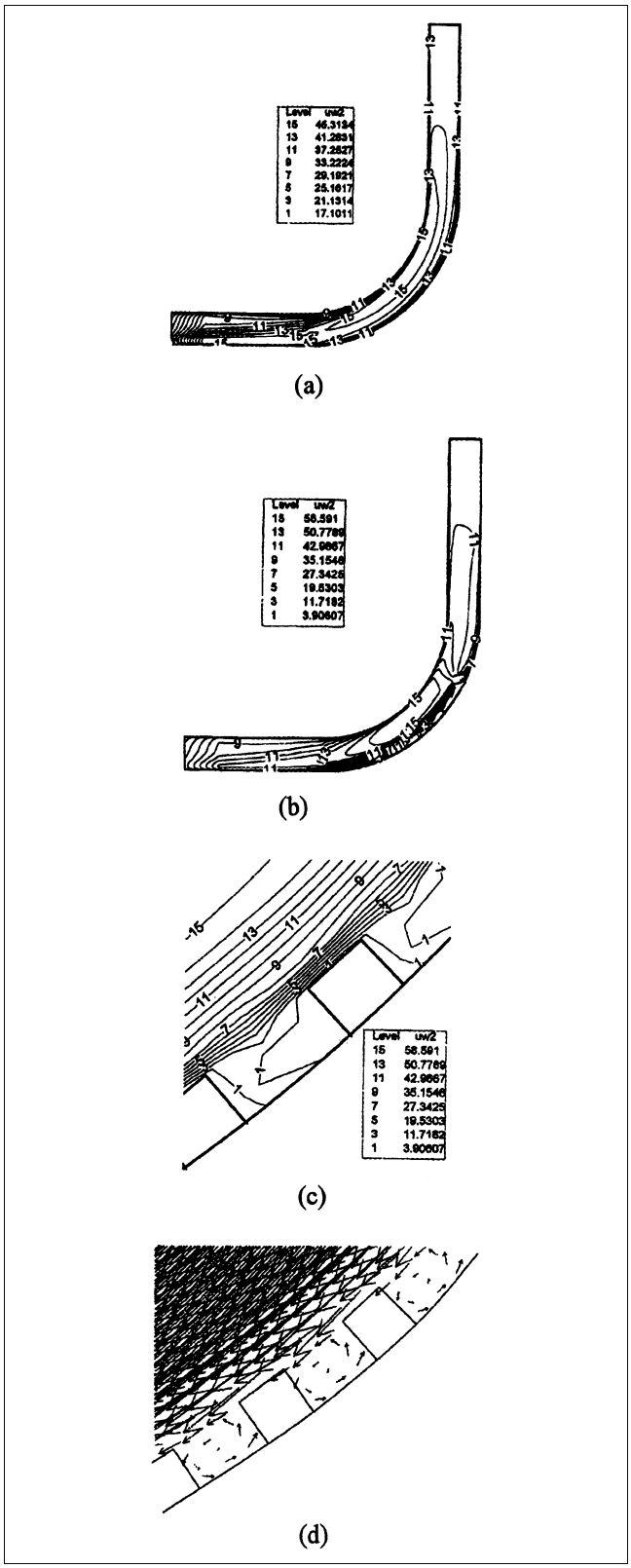

Figure 5. Axial gas field: ribbed bend (B1) vs. bare bend.

(a) Contour of velocities in bare bend; (b) contour of velocities in B1; (c) contour of velocities at interval of ribs in B1; (d) vectors of velocities at interval of ribs in B1.

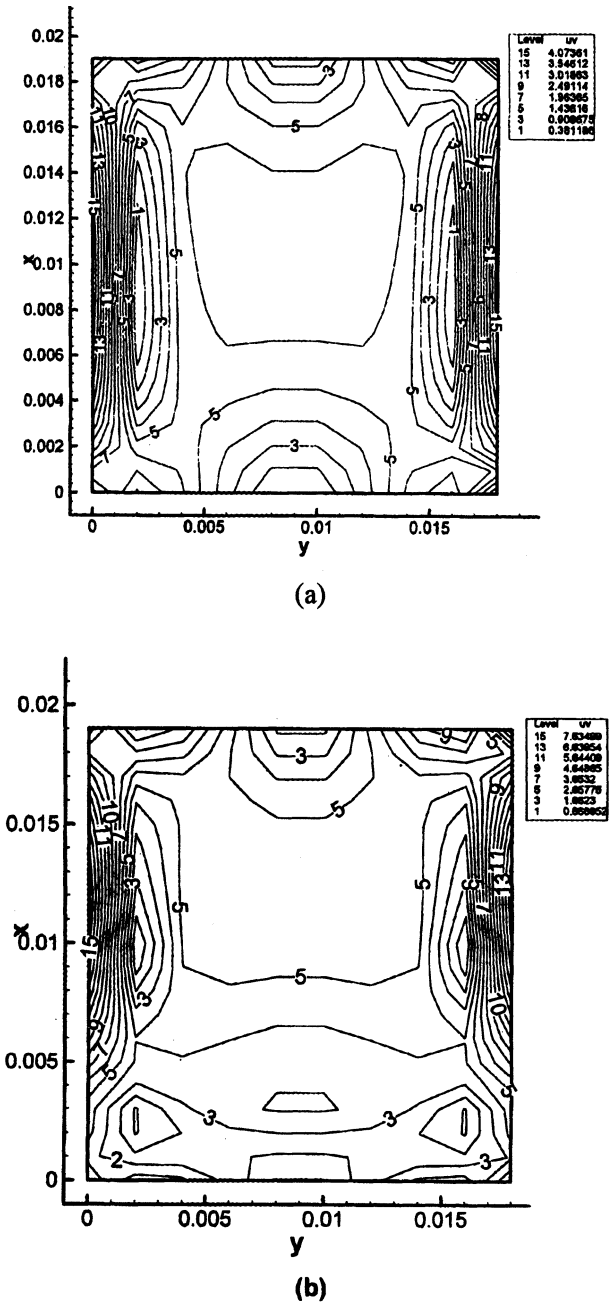

Figure 6. Secondary flow: ribbed bend (B1) vs. bare bend at 45° cross-section: (a) contour of velocities in bare bend; (b) contour of velocities in B1.

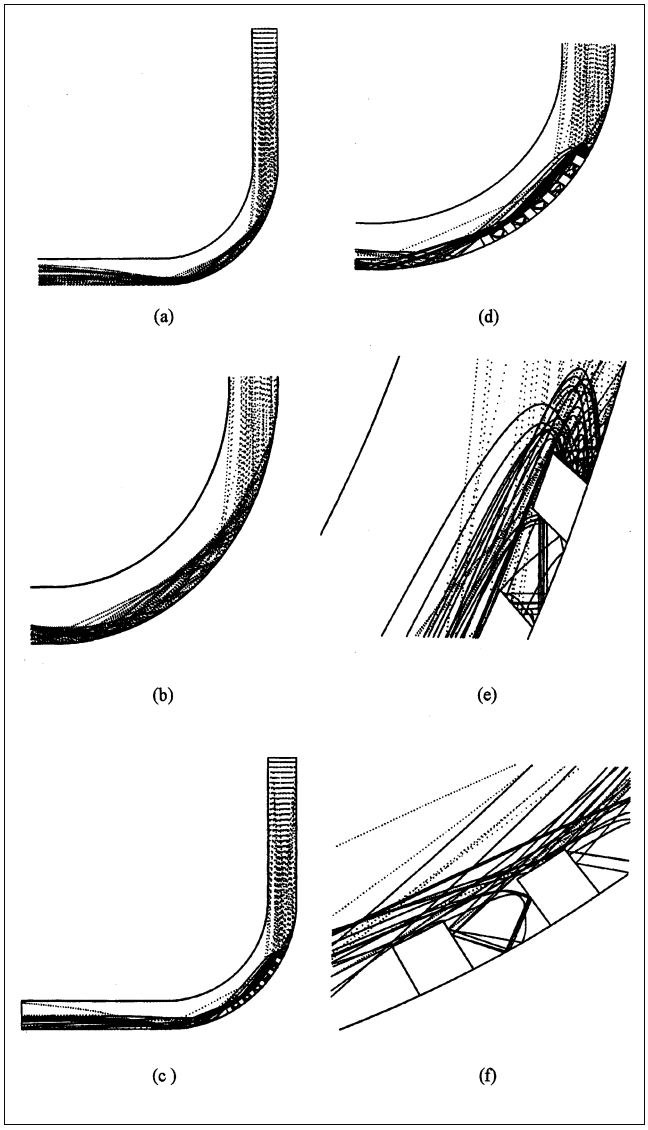

Figure 7. Particle trajectory: ribbed bend (B1) vs. bare bend.

(a) Particles trajectory throughout the bare bend; (b) particles trajectory in the bend part of bare bend; (c) particles trajectory throughout B1; (d) particles trajectory in the bend part of B1; (e) particles trajectory against the first rib of B1; (f) particles trajectory against the last rib of B1.

usually follow very complicated trajectories. The rebounding particles with low residual speed will probably hit the rib surface again and again with decaying speed, and eventually slide down to the bend wall. Particles with high rebounding speed, however, may impact on the bend wall and rebound, hitting the back of the previous rib repeatedly.

Particles that make tertiary impacts have different trajectories, depending on the speed and angle of their rebound. With sufficiently high rebounding momentum and a suitable rebounding angle, particles will either enter the bulk flow beyond the ribs and are swept out quickly, or they will settle on the wall as a result of particle–turbulence interaction.

Most particles in a ribbed bend impact the metal surface more than once. Therefore, their path in the bend usually consists of a series of rib–wall–rib impacts before they finally leave the ribbed area with the bulk gas flow. Erosion caused by rib–wall–rib impacts is insignificant. As confirmed by both experimental and numerical studies, both the incidence angle and impact velocity of a particle are changed by the ribs.

Particles impact velocity

The effect of particle-impact velocity on the erosion rate is often described by a power-law correlation (particle velocity)^n, in which the power exponent is usually in the range $2 < n <$

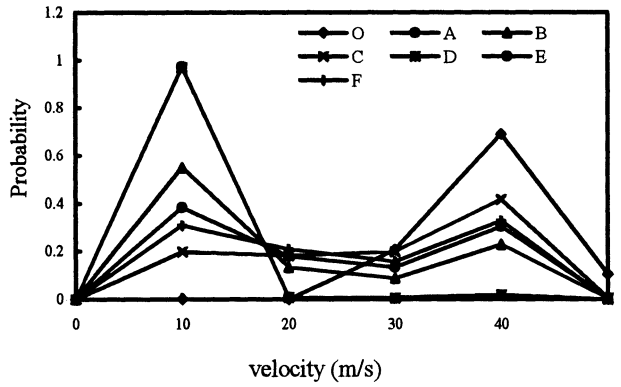

Figure 8. Particle–wall impact velocity distribution: ribbed bends vs. bare bend.

2.5 for ductile materials, while for brittle materials, it can be much larger (Mason and Smith, 1972).

In the present work, all impact velocities are recorded in several different ranges: 0 ~ 10 m/s, 10 ~ 20 m/s, 20 ~ 30 m/s, 30 ~ 40 m/s, and 40 m/s or higher. For the bare bend, the particle–wall impact velocity falls in the 30–40 m/s range, while no collisions are detected with an impact velocity lower than 20 m/s, as shown in Figure 8. For the ribbed bends, particle–rib and particle–wall impacts are considered separately. Over the parameter ranges tested in this work, particle–rib impact velocity is found to fall in the 0–10 m/s range, with a probability higher than 99%. In comparison with the bare bend, it can be concluded that most particle–rib impacts occur with low velocity. Moreover, in the ribbed bends, particles are very likely to impact on the bend wall with an impact velocity of 0–20 m/s. For case A and case D ribbed bends, more than 90% of particle–wall impacts have an impact velocity of 0–10 m/s.

Figure 9 further compares the normalized impact velocity distribution of particle–wall impacts (per unit time) between ribbed and bare bends, where N is the occurrence (per unit time) of particle–wall impacts with an impact velocity that falls into a certain range, while N_0 refers to that for the bare bends. The ratio N/N_0 indicates the difference between ribbed and bare bends in terms of impact-velocity distribution.

Figure 9a shows that the ratio N/N_0 for the bare bends is much higher than that for the ribbed bends. Figures 9b and 9c suggest similar trends. It is therefore obvious that particle–wall impacts in a bare bend are far more likely to occur with a high impact velocity (> 20 m/s) than in a ribbed bend. Actually, in our numerical predictions no particle–wall impact occurred with a velocity less than 20 m/s for the bare bends.

Obviously, for the ribbed bends, the impact velocity between particles and surface (particle–rib or particle–wall) tends to be low. This lower impact velocity is one reason why the erosion rate of the ribbed bends is low in comparison with that of the bare bends.

Particles impact angle

The impact angle also strongly affects the erosion rate. Brittle materials are highly resistant to oblique impact and

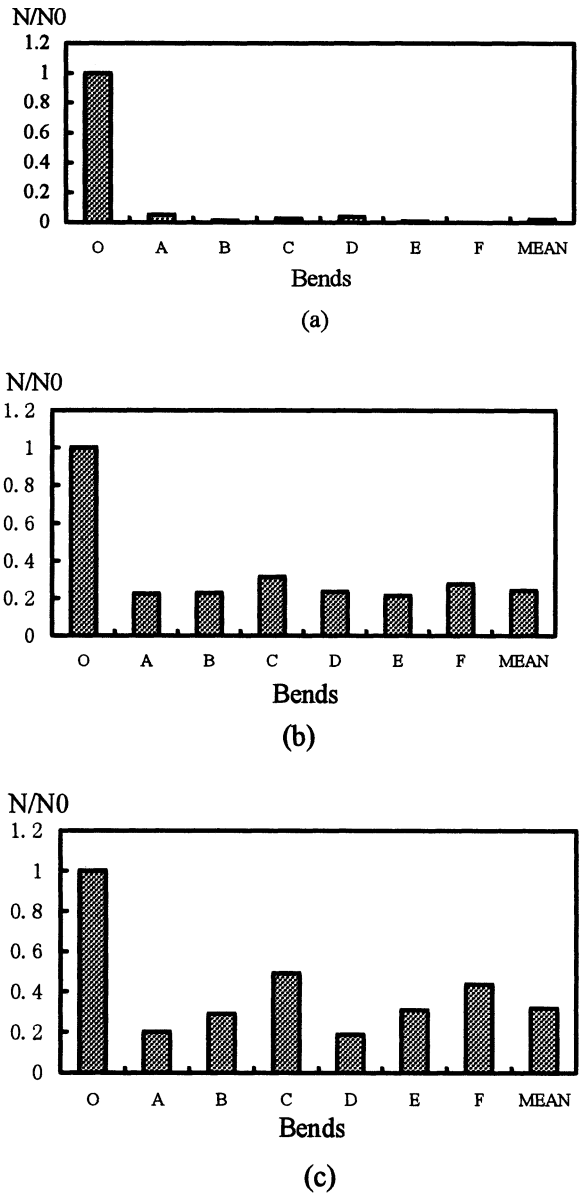

Figure 9. Particle–wall impact velocity relative distribution: ribbed bends vs. bare bend.

(a) > 40 m/s; (b) 30 ~ 40 m/s; (c) 20 ~ 30 m/s.

suffer most from the particle stream at high angles of incidence. For ductile materials, the maximum erosion occurs at a relatively low angle of incidence. In the present article, both in the experiments and the prediction, the material involved is medium carbon steel, which is considered a ductile material. According to previous studies by Finnie (1960), Tilly (1969), and Cousen and Hutchings (1983), maximum erosion occurs at an incidence angle of 20°–30° for such materials.

It is helpful to look at the difference in impact angle distribution between ribbed and bare bends, especially in the 20°–30° range. As suggested earlier, both particle–rib and particle–wall impacts are examined.

In all cases of particle–rib impacts, the probability that particles will impact at an angle of 20°–30° is only 1%–4%, with an average of 2.28%. Most impacts are found to occur

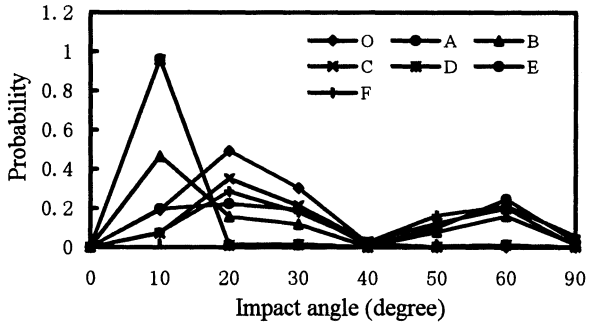

Figure 10. Particle–wall impact angle distribution: ribbed bends vs. bare bend.

with a greater angle of incidence. Particle–wall impact angle distribution differs significantly. Figure 10 shows that for bare bends the impact angle falls mostly in the range of 20°–30° and that collisions almost never occur at 40°–90°. In ribbed bends there is a higher probability that the impact angle will occur at three angles of incidence: 0°–10°, 10°–20°, and 50°–60°. For ribbed-bend cases A and D in particular, more than 90% of the impacts occur at an incidence angle of less than 10°.

Figure 11 compares the particle–wall impact-angle distributions (per unit time) between the ribbed and bare bends. Just as before, N refers to the number of particle–wall impacts occurring per unit time for a certain interval of incidence angle, while N_0 refers to that for only the bare bend. Figure 11a suggests that the relative value of N/N_0 for cases A and D is much higher than that for the bare bends, but for case B, it is only slightly higher than that for the bare bends. Figures 11b–11d compare particle–wall impact-angle distribution in more detail. As expected, the relative value of N/N_0 for all ribbed bends is lower than that for the bare bends.

From the preceding discussion, we can see that the relative value (N/N_0) for cases C, E, and F ribbed bends is lower than that for bare bends over the 0°–40° range, but higher at larger incidence angles. It can be concluded that particle–surface (including particle–rib and particle–wall) impacts tend to occur at medium impact angles when ribs are added to the outer wall of an inside bend, which is important evidence of the erosion-protecting effect of ribs.

Comparison of erosion rates

Figure 12 compares the predicted erosion rates for ribbed and bare bends. The average erosion rate for all the ribbed bends tested is only 34% of that for the bare bend, suggesting a 66% reduction. The lifetime service of the bare bends can be extended three times by proper ribbing.

In the test, there are six kinds of rib, with different cross sections, A, B, C, D, E, F, corresponding to 5×5, 4×4, 3×3, 5×2.5, 4×2, 3×2. Taking the relationship between rib shape and erosion into consideration, the present article compares the erosion of ribs with different cross sections, requiring only that their arrangement be equal.

From Figure 12, which compares the erosion rate of square cases A, B, C with that of rectangular cases D, E, F, respectively, we can see clearly that rectangular ribs have a greater antierosion effect than do square ribs.

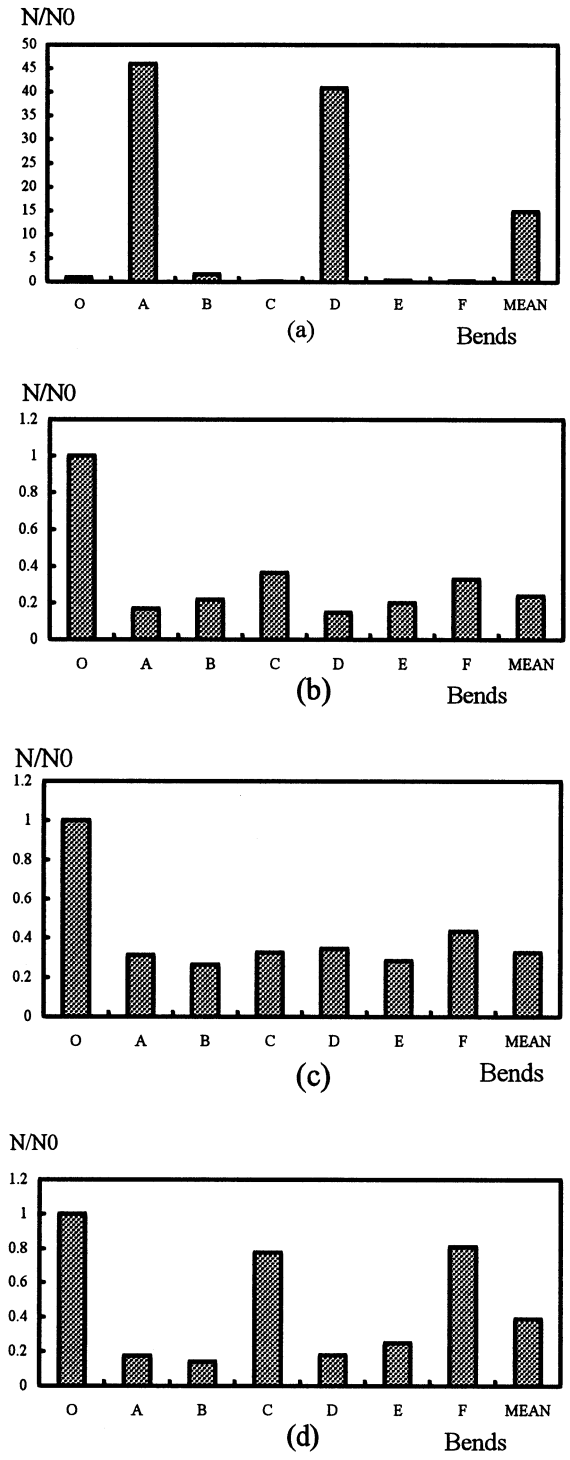

Figure 11. Particle–wall impact angle relative distribution: ribbed bends vs. bare bend.

(a) 0° ~ 10°; (b) 10° ~ 20°; (c) 20° ~ 30°; (d) 30° ~ 40°.

In the present work, the erosion rates of the ribs and the bend walls are calculated separately. For example, for case A1, the erosion rate of the five ribs is computed separately from that of the bend wall, which allows us to see the difference in erosion rate between ribs and the bend wall.

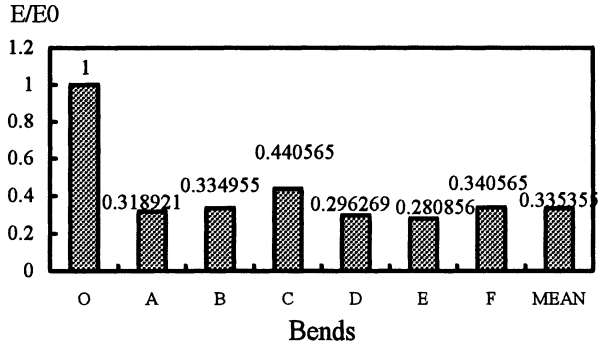

Figure 12. Erosion rate: ribbed bends vs. bare bend.

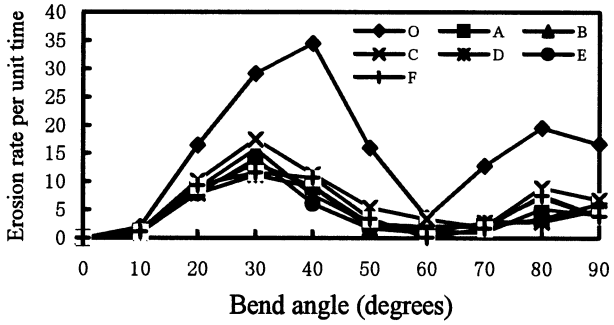

Figure 14. Erosion distribution on the outer wall: ribbed bends (sum of ribs and the wall) vs. bare bend.

Figure 13 compares the erosion rates of the ribs and the bend wall for all ribbed bends. Erosion of the ribs is significantly lower than that of the bend wall. When we examined the mean erosion rate of all the ribbed bends, we found that the rib erosion rate (E_f) is only 30.4% of the total erosion rate, while the wall erosion rate (E_w) accounts for the remaining 69.6%, more than twice of the former.

Wear distribution

Figure 14 shows the wear distribution along the outer wall of the inside bends. Two peak values of the erosion rate are found along the wall in all the cases examined. For the bare bend, the first peak is located at about 40° incidence angle while the second, smaller one is at around 80°. Analysis of the particle trajectories in the first case shows that the two main points of erosion along the outer bare bend are caused by the primary and secondary particle impacts, both at high impact velocity and sharp incidence angle. For the ribbed bends, all of the wear occurs mostly in the zone between 30° and 80°. In comparison with the bare bend, even the peak values of the erosion rate for ribbed bends are much lower. Interestingly, the point of least wear for both bare and ribbed bends occurs at about 60° incidence angle. It can therefore be concluded that proper ribbing can substantially reduce the erosion rate, although it does not effect a change in the pattern of wear distribution.

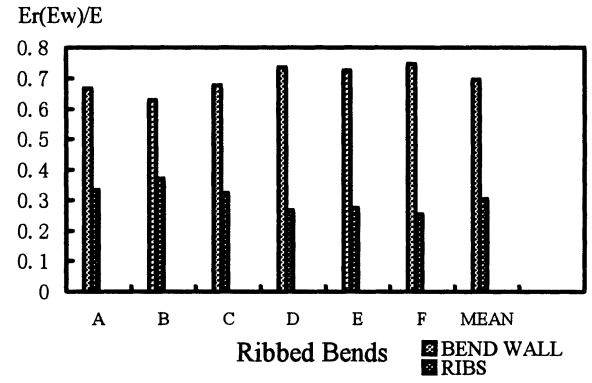

Figure 13. Erosion rate: ribs vs. bend wall in ribbed bends.

Reasons for erosion protection by ribbing

As a gas–solid flows through a bend, particles impact on the wall by inertia and centrifugal force. High-speed particles will not only cause impingement erosion on the wall, but also cause abrasive erosion on the wall by sliding and rolling on the metal surface. Adding ribs on the wall can alter this situation. First, ribs can alter the particle impact angle and speed, and decrease the chance of direct impact on the wall. The impact history of most particles in a ribbed bend is a series of rib–wall–rib impacts. The first impact usually occurs on the rib at a high speed but medium angle, the second one occurs on the bend wall at a reduced speed and altered angle, and the third impact is likely to occur on the back of the previous rib at an even lower speed and medium angle. Consequently, the erosion caused by rib–wall–rib impacts is fairly low, because both the incidence angle and impact velocity are greatly changed by the ribs. Second, ribs will prevent particles from sliding and rolling along the metal surface, change the flow direction, and make the particles settle on the bend wall.

Conclusions

The following conclusions can be drawn from the preceding discussion:

1. Both experiments and numerical simulations demonstrate that adding ribs to the outer wall of the inside bend can greatly reduce its erosion rate. Under test conditions, the average ribbed-bend erosion rate is only a third of that of the bare bend. Moreover, both results suggest that rectangular ribs have more of an antierosion effect than do square ribs.

2. The numerical prediction of gas flow and particle trajectory provides a better understanding of the underlying mechanism of erosion reduction by ribs. Axial gas flow along the bend has much more of an effect on determining the particle trajectory than the secondary flow at the cross section does. The impact history of most particles in a ribbed bend is usually a series of rib–wall–rib impacts. Erosion is reduced by the decreased impact velocity and altered incidence angle.

3. The present numerical results show that, for a ribbed bend, the particle–surface impact velocity (including particle–rib and particle–wall) tends to be lower compared to that in a bare bend. Almost all of the particle–rib impacts occur at an impact velocity of less than 10 m/s. For particle–wall impacts, up to 10% of the impacts can happen with an im-

pact velocity between 10 m/s and 20 m/s. For a bare bend, however, the impact velocity is almost never less than 20 m/s over the parameter range examined.

4. Numerical results also show that the incidence angle of particle–surface impacts tends to occur in the medium range. In some cases examined (that is, cases A and D), more than 90% of the impacts occurred with an incidence angle of less than 10°. But for the bare bend, the impact angle occurs largely in the 20°–30° range.

5. Numerical predictions indicate that bend-wall erosion is more serious than when ribs are present. By adding ribs, the pattern of wear distribution remains much the same, although the erosion rate can be substantially reduced.

The numerical results are in excellent agreement with the experimental data. However, the present article is only concerned with some basic aspects of the ribbed bend. This justifies further study involving more complex geometric configurations. It was noted in this work that the ribbed bends with low erosion rates have a turbulent "stagnant" zone in gas flow in the vicinity of the ribs that may affect the transport capacity of the pneumatic conveying line. A balance between transport capacity and equipment lifetime needs in-depth investigation to determine the influence of ribs on the hydrodynamics in a bend.

Acknowledgment

This project was supported by National Natural Science Foundation of China (No: 29876034).

Literature Cited

Cousen, A. K., and I. M. Hutchings, *Proc. Int. Conf. on Erosion by Liquid and Solid Impact*, (1983).

Crowe, C. T., M. P. Sharma, and D. E. Stock, "The Particle-Source-in-Cell (PSI-Cell) Model for Gas-Droplet Flows," *J. Fluids Eng.*, **99**, 325 (1977).

Fan, J. R., D. D. Zhou, K. L. Zeng, and K. F. Cen, "Numerical and Experimental Study of Finned Tube Erosion Protection Methods," *Wear*, **152**, 1 (1992).

Fan, J. R., X. Y. Zhang, L. H. Chen, and K. F. Cen, "New Stochastic Particle Dispersion Modeling of a Turbulent Particle-Laden Round Jet," *Chem. Eng. J.*, **66**, 207 (1997).

Finnie, I., "Erosion of Surfaces by Solid Particles," *Wear*, **3**, 87 (1960).

Finnie, I., "Some Observations on the Erosion of Ductile Metals," *Wear*, **19**, 81 (1972).

Grant, G., and W. Tabakoff, "Erosion Prediction in Turbomachinery Resulting from Environmental Solid Particles," *J. Aircraft*, **12**, 471 (1975).

Humphrey, J. A. C., "Fundamentals of Fluid Motion in Erosion by Solid Particle Impact," *Int. J. Heat Fluid Flow*, **11**, 170 (1990).

Launder, B. E., and D. B. Spalding, "The Numerical Computation of Turbulent Flows," *Comput. Methods Appl. Mech. Eng.*, **3**, 269 (1974).

Mason, J. S., and B. V. Smith, "The Erosion of Bends by Pneumatically Conveyed Suspension of Abrasive Particles," *Powder Technol.*, **6**, 323 (1972).

Patankar, S. V., *Numerical Heat Transfer and Fluid Flow,* McGraw-Hill, New York (1980).

Sommerfeld, M., and G. Zivkovic, "Recent Advances in the Numerical Simulation of Pneumatic Conveying Through Tube Systems," *Comput. Methods Appl. Sci.*, **21**, 201 (1992).

Song, X. Q., J. Z. Lin, J. F. Zhao, and T. Y. Shen, "Research on Reducing Erosion by Adding Ribs on the Wall in Particulate Two-Phase Flows," *Wear*, **193**, 1 (1996).

Tabakoff, W., R. Kotwal, and A. Hamed, "Erosion Study of Different Materials Affected by Coal Ash Particles," *Wear*, **52**, 161 (1979).

Tilly, G. P., "Erosion Caused by Airborne Particles," *Wear*, **14**, 63 (1969).

Tilly, G. P., "Erosion Caused by Impact of Solid Particles," *Treatise Mater. Sci. Technol.*, **13**, 287 (1979).

Yao, J., B. Z. Zhang, and J. R. Fan, "An Experimental Investigation of a New Method for Protecting Bends From Erosion in Gas–Solid Flows," *Wear*, **240**, 215 (2000).

Manuscript received Sept. 18, 2000, and revision received Nov. 27, 2001.